

Thermal transport in CuCr_2X_4 ($X = \text{S, Se, Te}$): Experiment and *ab initio* calculationsKyo-Hoon Ahn ¹, Miroslav Soroka ^{1,2,3}, Petr Levinský ¹, Karel Knížek ^{1,*}, Jiří Hejtmanek ¹,
Vladimír Kucek ⁴ and Jiří Navrátil ⁴¹*Institute of Physics of the CAS, Cukrovarnická 10, 162 00 Praha 6, Czech Republic*²*Institute of Inorganic Chemistry of the Czech Academy of Sciences, 250 68 e, Czech Republic*³*Charles University, Faculty of Science, 128 43 Prague 2, Czech Republic*⁴*University of Pardubice, Faculty of Chemical Technology, Studentská 573, 532 10 Pardubice, Czech Republic* (Received 27 January 2021; revised 13 June 2021; accepted 6 August 2021; published 24 August 2021)

We present a combined experimental and theoretical study of the longitudinal and transverse thermoelectric properties of ferrimagnetic spinels CuCr_2X_4 ($X = \text{S, Se, Te}$). The thermoelectric power of all studied phases is positive and consists of two contributions; an almost linear diffusive thermopower observed at high temperature, and a strong enhancement below T_C attributed to magnon drag. The diffusive part of thermopower and resistivity decreases from $X = \text{S}$ to Te , whereas the magnon drag enhancement is the biggest for $X = \text{Se}$, which has also the highest T_C . The thermopower was calculated by DFT method using GGA, GGA + U , GGA+oeHyb, and mBJ potentials. A good agreement with the experimental thermopower was achieved using GGA potential for $X = \text{S}$ and with mBJ potential for $X = \text{Te}$. The mBJ potential, which was designed for sp -type semiconductors, better describes the valence bands of CuCr_2Te_4 that exhibit stronger sp -orbitals character than sulfide and selenide. The anomalous Nernst effect (ANE) is negative at room temperature for all phases, the highest absolute value $\sim 1.5 \mu\text{V}/\text{K}$ is observed for $X = \text{Te}$ and Se around room temperature, whereas ANE for $X = \text{S}$ is much smaller. A sign change of ANE to positive is observed at 285 K for $X = \text{S}$ and at 65 K for $X = \text{Se}$. The trend of anomalous Nernst conductivity is reproduced by Berry phase calculations if the renormalization of the bands due to the strong correlation effects is taken into account.

DOI: [10.1103/PhysRevB.104.085146](https://doi.org/10.1103/PhysRevB.104.085146)**I. INTRODUCTION**

Recent studies of phenomena arising from the coupling between spin and heat currents as well as types of anomalous Hall effects (AHE) in various magnetic materials have triggered renewed interest in the anomalous Nernst effect (ANE) as one of the topologically nontrivial phenomena and for its potential application to thermoelectric devices. Interesting materials exhibiting this kind of phenomena could be found in the ferrimagnetic chalcogenide spinel series CuCr_2X_4 ($X = \text{S, Se, Te}$), where ANE and AHE were studied for $X = \text{Se}$ [1–6] and AHE for $X = \text{S}$ [7]. The CuCr_2X_4 phases exhibit long range magnetic ordering below $T_C \sim 380, 430, \text{ and } 325 \text{ K}$ for $X = \text{S, Se, and Te}$, respectively, with saturated magnetic moment at low temperature around $5 \mu_B$. It was found that the behavior of AHE and ANE in CuCr_2Se_4 corresponds to the intrinsic mechanism explained by Karplus-Luttinger theory and its modern generalization based on the Berry-phase approach [2,4,8]. We assume that the same approach can be applied for CuCr_2S_4 and CuCr_2Te_4 . In order to analyze the transverse transport properties, it is helpful to investigate also the longitudinal transport properties, linked together by the Onsager relations [9–11]. As regard the temperature dependence of thermopower in CuCr_2X_4 , in addition to the diffusive contribution described by Mott formula [12], a strong enhancement

at lower temperature is observed pointing to a strong influence of magnons and their dynamics [13,14].

The charge and spin density transfer between cations and ligands markedly influences the character of bands at the Fermi level and consequently the transport properties. The magnetic structure and moments on individual sites were studied by neutron diffraction in CuCr_2Se_4 and CuCr_2Te_4 . The former studies found a magnetic moment on Cr site between $2.8\text{--}3 \mu_B$ and zero moments on remaining sites, thus claiming a ferromagnetic ordering [15,16]. A similar conclusion was also derived in a later study [17]. This value of Cr magnetic moment would correspond in an ideal case to electron configuration d^3 , valency Cr^{3+} , and spin magnetic moment $3 \mu_B$. The corresponding valency distribution model is $\text{Cu}^{2+}\text{Cr}_2^{3+}\text{Se}_4^{2-}$. The neutron diffraction on CuCr_2Te_4 revealed that magnetic moment on Cr site is enhanced to $3.11 \mu_B$ compared to CuCr_2Se_4 [16]. On the other hand, Yamashita *et al.* refined a smaller magnetic moment on Cr site $2.64 \mu_B$ and negative moments on Cu and Se -0.07 and $-0.2 \mu_B$, respectively, thus claiming a ferrimagnetic ordering [18]. That would correspond in an ideal case to valency distribution $\text{Cu}^{1+}\text{Cr}_2^{3.5+}\text{Se}_4^{2-}$ and Cr electron configuration $d^{2.5}$. In the present work we confirm by electronic structure calculation the latter case, i.e., ferrimagnetic ordering with small negative moments on Cu and Se.

In this work we have focused on the comparison of the experimentally determined transverse and longitudinal transport properties of CuCr_2X_4 ($X = \text{S, Se, and Te}$) with the

*Corresponding author: knizek@fzu.cz

calculated properties obtained using the electronic structure calculation based on the density functional theory (DFT). The thermoelectric power was calculated using the BOLTZTRAP program [19]. Anomalous Nernst conductivity was reproduced by Berry phase calculations. The magnetic moments and oxidation states were evaluated by atoms in molecules approach [20].

II. COMPUTATIONAL METHOD

We performed density-functional theory (DFT) calculations using the WIEN2K package [21], implementing the augmented plane wave and local orbital (APW + lo) method. The generalized gradient approximation (GGA) [22] is employed for the exchange-correlation potential. The structural parameters are fully optimized in GGA level, resulting in $a = 9.9040, 10.4352, 11.2310$ Å and $x = 0.2583, 0.2578, 0.2573$ of the X site (x, x, x) in $Fd\bar{3}m$ space group, for S, Se, and Te, respectively. The muffin-tin radii of 2.3, 2.3, 1.8, 2.0, and 2.3 a.u. (a.u. = Bohr radius = 0.529 Å) are used for the Cu, Cr, S, Se, and Te atoms. The maximum modulus for the reciprocal vectors K_{\max} was chosen such that $R_{\text{MT}} \times K_{\max} = 8.0$. The Brillouin zone was sampled with $20 \times 20 \times 20$ mesh.

To investigate the effects of exchange-correlation functional, modified Becke-Johnson (mBJ) potential [23], GGA, GGA + U , and GGA plus on-site exact-exchange hybrid (GGA+oeHyb) functional [24] are used in this paper. The mBJ has an orbital independent exchange-correlation potential (not functional) from the original Becke-Johnson terms [25]. While this approach improves especially the sp characters, the methods described below focus on d and f shells only. The GGA + U approach is carried out for the strong correlation effects of the $3d$ electrons at Cu and Cr sites. Here the fully localized limit (FLL) [26] is chosen for the double-counting method using the effective Hubbard parameter defined by $U_{\text{eff}} = U - J$ with $J = 0$. The calculations with the oeeHyb functional are also executed as a comparison. The exact (Hartree-Fock) exchange is applied to the correlated $3d$ shells with full anisotropy of the exchange, replacing 20% of the local density exchange by the exact one.

The Seebeck coefficients were carried out using semi-classical Bloch-Boltzmann transport theory with the constant scattering time approximation, implemented in the BOLTZTRAP code [19]. The Brillouin zone was sampled with a dense k mesh up to $60 \times 60 \times 60$, and the grid were interpolated onto a grid containing eight times as many k points.

To extract the Berry-phase effect in thermoelectric transport, model Hamiltonians which reproduce the energy range of -7 to 4 eV are constructed using WIEN2WANNIER [27] and WANNIER90 [28] packages. The basis was composed of d orbitals at each Cu and Cr site and p orbitals at X site. The anomalous Hall conductivity (AHC) σ_{xyz} and the anomalous Nernst conductivity (ANC) α_{xyz} can be expressed with the out-of plane component $\Omega_{n,z}(\mathbf{k})$ of the Berry curvature as follows [4]:

$$\sigma_{xyz}(T, \mu) = -\frac{e^2}{\hbar} \int \frac{d\mathbf{k}}{(2\pi)^3} \Omega_{n,z}(\mathbf{k}) f_{n\mathbf{k}}, \quad (1)$$

$$\alpha_{xyz}(T, \mu) = -\frac{1}{e} \int d\varepsilon \left(-\frac{\partial f}{\partial \varepsilon} \right) \sigma_{xyz}(0, \varepsilon) \frac{\varepsilon - \mu}{T}, \quad (2)$$

where e , \hbar , $f_{n\mathbf{k}}$, ε , and μ are the elementary electric charge, the reduced Planck constant, the Fermi-Dirac distribution function with the band index n and the wave vector \mathbf{k} , the band energy, and the chemical potential, respectively. To check the convergence of σ_{xyz} , a dense k mesh of $300 \times 300 \times 300$ ($500 \times 500 \times 500$) is used for Se/Te (S) [29]

In the electronic structures of CuCr_2X_4 , the d bands of Cu/Cr sites and the p bands at X sites are distributed over the range from -7 to 4 eV. To calculate the anomalous Hall conductivity by Eq. (1), the integration of the Berry curvature is started from the bottom of the bands, which is at -7 eV. It means that the model Hamiltonian should reproduce the DFT band structure correctly, not only around the Fermi energy, but also the bottom of the bands.

The atomic charges and magnetic moments were calculated using the atoms in molecules (AIM) concept of Bader [20]. In this approach, the unit cell is divided into regions by surfaces that run through the minima in the charge density. By integrating the electron or spin density within these regions the charge or spin moment on a given site can be calculated. The advantage of this method is that the analysis is based solely on the charge or spin density so it is independent on the basis set and atomic spheres used.

III. EXPERIMENT

Bulk polycrystalline samples of the CuCr_2X_4 ($X = \text{S, Se, Te}$) compounds were prepared through the solid state chemical reaction route using elemental Cu (Sigma-Aldrich 4N), Cr (Sigma-Aldrich 4N), S (Sigma-Aldrich 5N), Se (Sigma-Aldrich 5N), and Te (Sigma-Aldrich 5N) in stoichiometric amounts. The mixture of the elements was sealed in evacuated quartz tubes and heated up to 800°C for about two (CuCr_2Te_4) to seven days (CuCr_2S_4) for the initial reaction. A very slow increase of temperature ($\sim 50^\circ\text{C}/\text{day}$ between 550 – 800°C) was used in case of CuCr_2S_4 compound to avoid explosion of the reaction ampoules. After this step the ampoules were slowly cooled and the mixtures were grounded to a powder, pelletized under 6 tons pressure and finally sintered for 72 h at 600°C .

The Nernst effect was measured using a homemade apparatus employing the standard setup in which the directions of magnetic field B_z , thermal gradient $\nabla_x T$, and resulting electric field E_y are mutually perpendicular. The thickness of the measured ceramic samples in the direction of the temperature gradient was $L_x = 2$ mm and the electric contact distance was $L_y = 4$ mm. The small voltage signal V_y was measured using a Keithley 2182A nanovoltmeter and the temperature difference ΔT_x was detected by differential thermocouples at the hot and cold sides of the samples. The magnetic field up to ± 8 kOe was changed in steps and data were acquired when the field was stable. The hysteresis loops were measured by starting and ending at the maximum positive field, and the temperature was changed while the field was at the maximum positive value. The Nernst signal S_{xyz} was calculated according to a

TABLE I. Calculated charges and spin moments in units of μ_B of CuCr_2X_4 . The analysis based on the atoms in molecules (AIM) theory is performed with AIM code implemented in WIEN2K package. The spin moments based on the atomic spheres and interstitial region are presented for comparison.

Method	X	Ionic charge/site (AIM)			Spin moment/site (AIM)			Spin moment/sphere			Spin moment/f.u.	
		Cu	Cr	X	Cu	Cr	X	Cu	Cr	X	Interstitial	Total
GGA+SOC	S	0.58	1.27	-0.78	-0.10	3.17	-0.30	-0.13	2.68	-0.10	0.24	5.05
	Se	0.42	1.09	-0.65	-0.08	3.36	-0.37	-0.12	2.78	-0.13	0.22	5.16
	Te	0.17	0.85	-0.47	-0.03	3.60	-0.43	-0.08	2.88	-0.13	0.28	5.45
mBJ+SOC	S	0.91	1.53	-0.99	-0.24	3.13	-0.25	-0.26	2.76	-0.11	0.20	5.02
	Se	0.73	1.36	-0.86	-0.14	3.29	-0.31	-0.17	2.84	-0.13	0.20	5.19
	Te	0.46	1.09	-0.66	-0.03	3.47	-0.35	-0.07	2.89	-0.12	0.25	5.50

formula¹

$$S_{xyz} = \frac{E_y}{\nabla_x T} = -\frac{V_y}{\Delta T_x} \frac{L_x}{L_y} (\mu\text{V/K}) \quad (3)$$

and was analyzed with respect to ordinary and anomalous effects, considering also the role of transverse thermal gradient $\nabla_y T$.

The low temperatures (2–310 K) measurements of electrical resistivity, thermopower (Seebeck coefficient $S_{xxz} = -V_x/\Delta T_x$), and thermal conductivity were made by the four-probe method of the thermal transport option (TTO) of the Physical Property Measurement System (PPMS, Quantum Design) by using a specimen of 8 mm length and $2 \times 2 \text{ mm}^2$ cross section. The Hall resistivity was measured using electrical transport option (ETO) of PPMS between -2 and 2 T, the thickness of the sample was $L_z = 0.5$ mm and the dimensions in the direction of electric current and detected voltage were $L_x = L_y = 4$ mm.

IV. RESULTS AND DISCUSSION

The calculated charges and spin moments are summarized in Table I. The calculated orbital moments are less than $0.01 \mu_B$, therefore we will just discuss the spin moments. Increasing degree of covalent character of the metal-ligand bond from $X = \text{S}$ to Te is manifested by lowering the calculated charges on individual sites. The calculated spin moments support the ferrimagnetic spin configuration for all CuCr_2X_4 phases with positive moment on Cr and negative moments on Cu and X sites. The absolute values of the moments on Cr and X sites are increasing from $X = \text{S}$ to Te , whereas moment of Cu is decreasing and for $X = \text{Te}$ the Cu spin moment is close to zero. The comparison with the charges and magnetic moments derived from the atom spheres revealed the importance of using the AIM (or similar) method for calculating both charges and spin moments in the case of CuCr_2X_4 phases, since a sizable spin moment exists also in

the interstitial region, which was mainly allocated to the Cr and ligand atoms by the AIM method.

Figures 1–3 show the electronic band structures of the ferrimagnetic phase of the three materials calculated using various potentials, namely GGA in Fig. 1, mBJ in Fig. 2, and GGA+oeeHyb in Fig. 3. Here the magnetization axis of the spin-orbit coupling (SOC) is set to the global (001) direction [30]. The effects of symmetry breaking by the SOC is clearly shown along Γ -X' (001), while it is smaller along Γ -X (100). It can be seen that the effect of SOC on the band structure is increasing from $X = \text{S}$ to Te . Since the behavior of the anomalous Hall and Nernst conductivity in CuCr_2Se_4 is consistent with the intrinsic mechanism and its generalization based on the Berry-phase approach [2,4,8], and a dominance of this mechanism in metallic ferromagnets with moderate electrical conductivity (typical conductivity for CuCr_2X_4 phases) is predicted [31], we expect that the same approach can be used for CuCr_2S_4 and CuCr_2Te_4 .

The experimentally determined temperature dependencies of thermopower and resistivity for CuCr_2S_4 , CuCr_2Se_4 , and

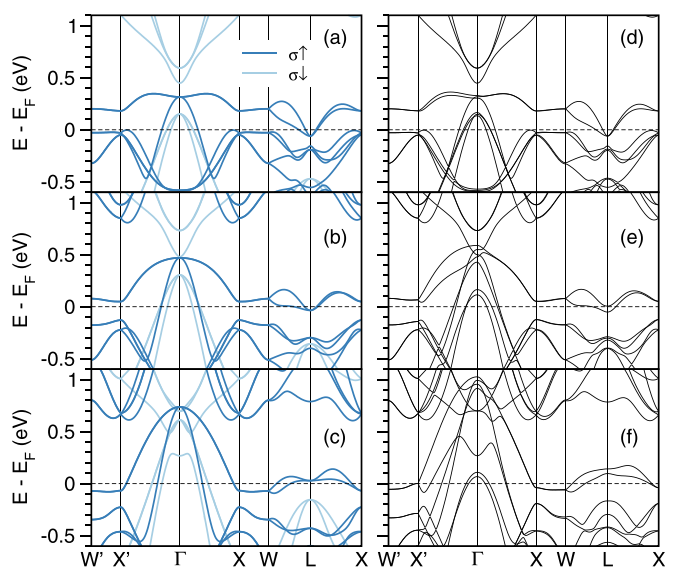


FIG. 1. Electronic band structures of ferrimagnetic (a) and (d) CuCr_2S_4 , (b) and (e) CuCr_2Se_4 , and (c) and (f) CuCr_2Te_4 , from the GGA calculations. The left and right panels are the results without and with SOC, respectively. The k path refers to Ref. [8].

¹Here we follow the convention of the three-index S_{xyz} , where the first index indicates the direction of the applied flux, the second index indicates the direction of the measured field, and the third index indicates the direction of the externally applied magnetic field, which is always z in our case. $V_y = V(y = L_y) - V(y = 0)$; $\Delta T_x = T(x = L_x) - T(x = 0)$.

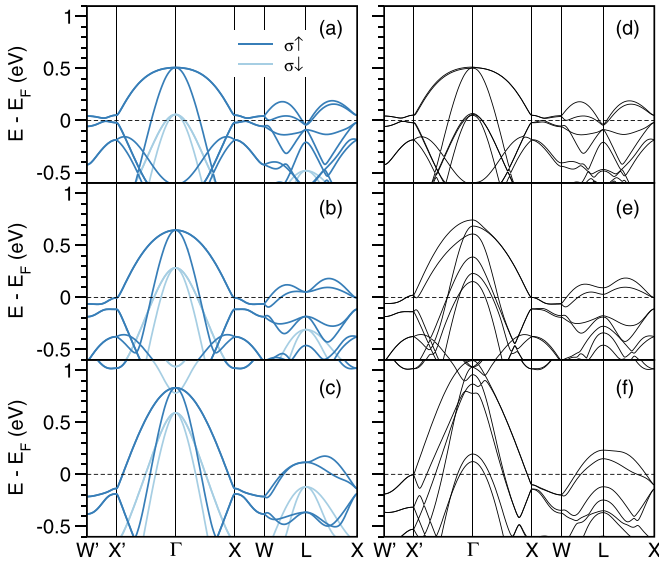


FIG. 2. Electronic band structures of ferrimagnetic (a) and (d) CuCr₂S₄, (b) and (e) CuCr₂Se₄, and (c) and (f) CuCr₂Te₄, from the mBJ calculations. The left and right panels are the results without and with SOC, respectively. The k path refers to Ref. [8].

CuCr₂Te₄ are presented in Fig. 4. The Seebeck coefficient is positive and converges to zero at low temperature for all three phases. Two contributions can be clearly distinguished in the thermopower temperature dependence. The almost linear thermopower at high temperature, and a strong enhancement at lower temperature. The practically linear part can be explained by a standard diffusive thermopower described by the Mott formula $S_d = \frac{\pi^2 k_B^2 T}{3e} \left(\frac{\partial \sigma}{\partial E} \right)_{E_F}$, where T is temperature, σ is electrical conductivity, k_B is the Boltzmann constant, and e is

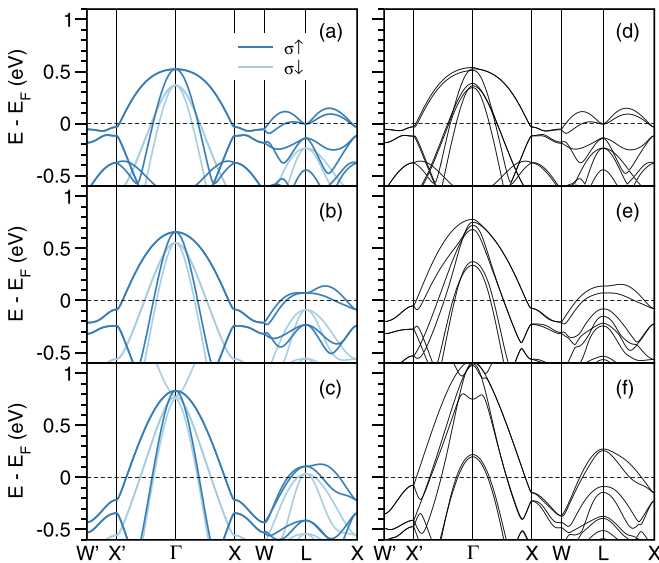


FIG. 3. Electronic band structures of ferrimagnetic (a) and (d) CuCr₂S₄, (b) and (e) CuCr₂Se₄, and (c) and (f) CuCr₂Te₄, from the GGA+oeeHyb calculations. The left and right panels are the results without and with SOC, respectively. The k path refers to Ref. [8].

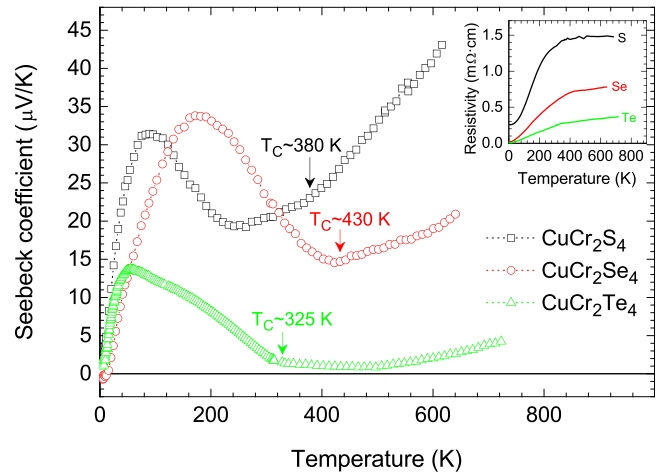


FIG. 4. Experimentally determined temperature dependence of thermopower for CuCr₂S₄, CuCr₂Se₄, and CuCr₂Te₄. The error bars are comparable to the size of the symbols. The ferrimagnetic ordering temperatures are indicated. The inset shows temperature dependence of electrical resistivity.

the charge of the carriers. A significant positive enhancement occurs just below T_C and could be assigned either to magnon or phonon drag. We interpreted it as magnon drag based on two key arguments. First, the onset occurs at the same temperature as the formation of the long-range ferromagnetic order for each phase. Phonon drag occurs typically at lower temperature. The second argument is the quite low observed thermal conductivity, see Fig. S1 in the Supplemental Material [32]. In connection with the relatively high metallic conductivity, the electronic contribution to thermal conductivity represents a significant part of the total thermal conductivity (with the exception of $X = S$), so the phononic part is below $2\text{--}3 \text{ W m}^{-1} \text{ K}^{-1}$. This observation disadvantages the phonon drag scenario due to the resulting short phonon mean free path. The magnon drag scenario was also supported in [13,14]. The diffusive thermopower is positive reflecting the hole character of charge carriers, and the magnon drag contribution is also positive. Magnon drag has the same sign as the diffusive thermopower, when the viscous hydrodynamic magnon drag, which lifts up the diffusing thermopower keeping the same sign, prevails over the effect of magnon decay, characterized by Gilbert damping parameter [33,34].

The magnitude of the diffusive part of thermopower is decreasing from $X = S$ to Te, similarly to resistivity. The magnon drag enhancement is the biggest for CuCr₂Se₄, which also has the highest T_C . The onset of magnon drag is quite steep making minimum at T_C in temperature dependence of thermopower for $X = S$ and Te. In the case of $X = S$ the growth of thermopower at T_C is slower and a steeper increase occurs at lower temperature. This behavior was reproduced for series of samples and it was also observed by other authors, see, e.g., Fig. 1 in Ref. [13] (let us remind that the labels of $X = S$ and Se for thermopower are exchanged in this figure). We do not have a definitive explanation for this behavior, but we tentatively ascribe it to small amount (around 5 mol %) of CuCrS₂ impurity present in all synthesized samples, and the resulting small local variations in stoichiometry. In our

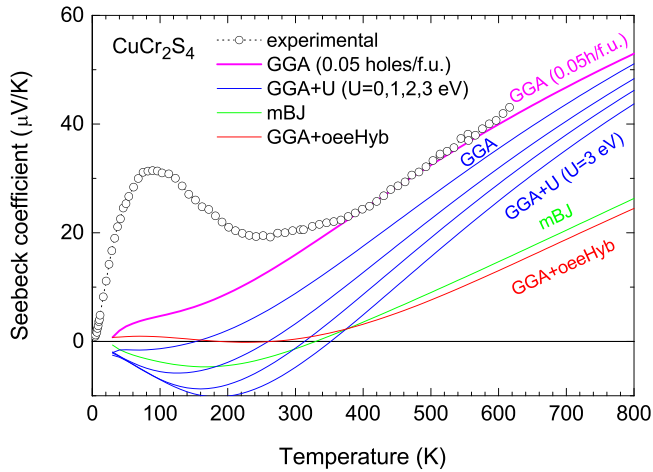


FIG. 5. Comparison of experimental and calculated thermopower of CuCr_2S_4 for various DFT potentials.

calculation we focus on the determination of the diffusive part of the thermopower by BOLTZTRAP code [19].

The comparison of experimental and calculated thermopowers of CuCr_2S_4 for various DFT potentials is shown in Fig. 5. We can see that the Seebeck coefficient based on GGA+oeeHyb and mBJ potentials is too low compared to experimental. Better agreement is achieved with GGA potential. Including GGA + U does not improve the situation, since the calculated thermopower is diminished with increasing U and becomes negative at lower temperature. The best agreement is achieved for calculation using a small shift of chemical potential achieved by introducing 0.05 holes *per* formula unit (f.u.) that would correspond to a slight off-stoichiometry like $\text{CuCr}_2\text{S}_{4.025}$. Comparing this calculated curve with the experimental data we can clearly distinguish the enhancement by magnon drag just below T_C at ~ 365 K.

The comparison of experimental and calculated thermopowers of CuCr_2Se_4 for various DFT potentials is shown in Fig. 6. In this case we could not find any suitable potential for describing experimental data. The curves based on GGA and GGA + U are close to observed data at high temper-

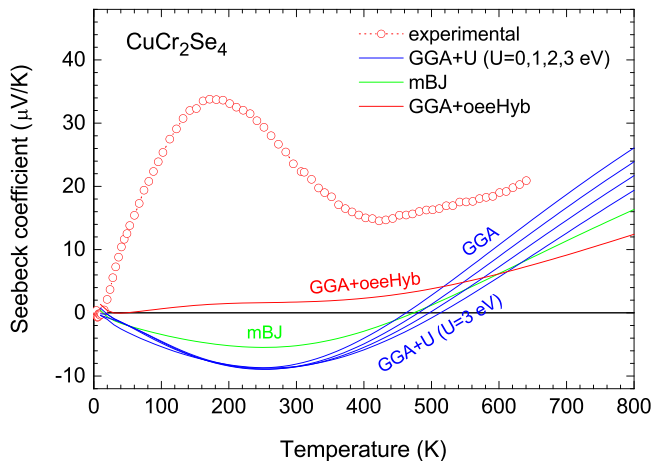


FIG. 6. Comparison of experimental and calculated thermopower of CuCr_2Se_4 for various DFT potentials.

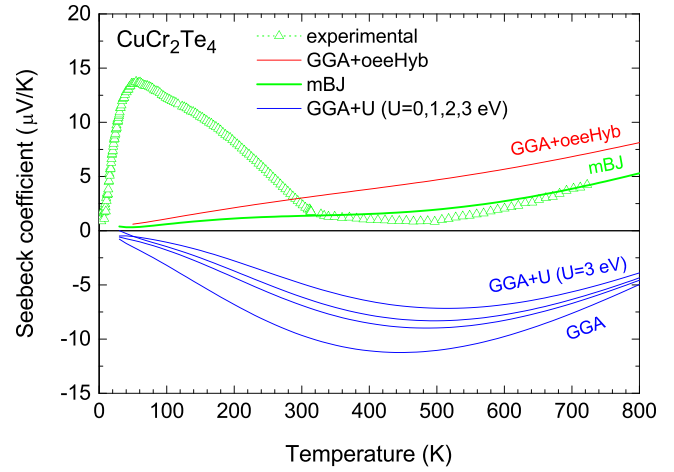


FIG. 7. Comparison of experimental and calculated thermopower of CuCr_2Te_4 for various DFT potentials.

ature, however they are shifted to negative values at lower temperatures. The curves based on GGA+oeeHyb displays better agreement at lower temperature but the increase at high temperature is too slow. The temperature trend of curve based on mBJ is intermediate between GGA and GGA+oeeHyb. Better agreement could be achieved, e.g., with GGA+oeeHyb calculation using a big shift of chemical potential achieved by introducing 0.3 electrons/f.u. (not shown). However, we consider this level of off-stoichiometry as unlikely in the present sample and, in addition, the rigid band approximation is not warranted to hold for such a shift of chemical potential.

The comparison of experimental and calculated thermopowers of CuCr_2Te_4 for various DFT potentials is shown in Fig. 7. In this case all curves based on the GGA or GGA + U potential are negative over the whole calculated temperature range. The curve calculated using the GGA+oeeHyb potential is positive, but it is significantly higher than the experimental one. The best agreement is achieved using the mBJ type of the potential. Although it does not exactly reproduce a small deflection in the experimental data with a minimum around 500 K, we consider this difference as negligible and the agreement as satisfactory. Comparing this calculated curve with the experimental data, we can again distinguish the enhancement by magnon drag below T_C at ~ 310 K.

In order to explain why the agreement is achieved for CuCr_2S_4 and CuCr_2Te_4 for different types of potentials, we will compare the character of bands at the Fermi level and the function of individual potentials. The studied phases contain transition metals Cu and Cr with partially occupied d orbitals, and ligand anions S, Se, or Te, for which the partially occupied valence orbitals have sp character. The bands at the Fermi level are mainly formed by d orbitals of Cr and sp orbitals of ligands, while the contribution of Cu d orbitals is smaller. The sp -orbitals character of the valence band is increasing with the increasing degree of covalency of the metal-ligand bond from $X = \text{S}$ to Te. The increasing covalency brings along the charge and spin density transfer from ligands to cations. This is clearly manifested by lowering the calculated charges on individual sites in Table I. The mBJ potential was developed to improve especially the band description and band gap in

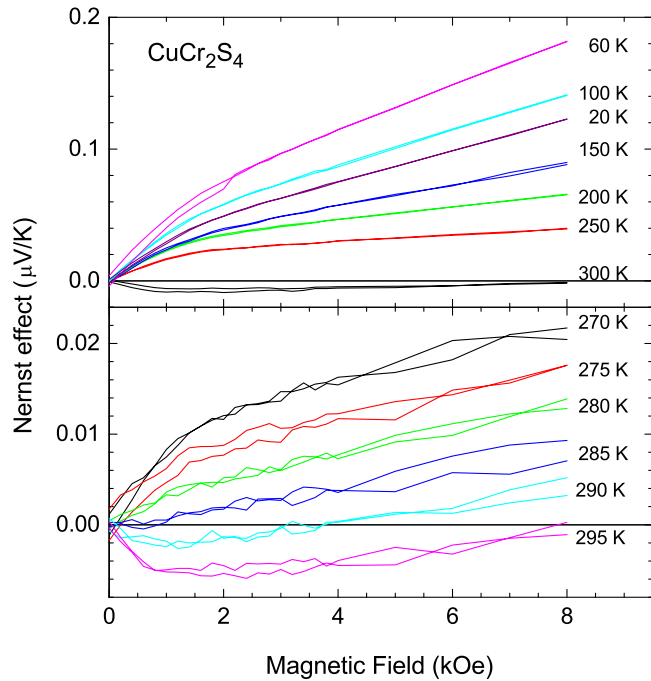


FIG. 8. Experimentally determined Nernst effect of CuCr_2S_4 for selected temperatures. The lower panel is focused on the sign change of ANE around 285 K.

semiconductors and insulators, where the valence and conduction band are prevalently of the sp -orbitals character [23]. Our results can be understood by considering that the sp -orbitals character of the valence band in CuCr_2Te_4 is so pronounced that the use of mBJ potential is valid. On the other hand, in CuCr_2S_4 with lower degree of covalency of the metal-ligand bond, the mBJ potential give less agreement with experiment than GGA potential. However, it seems that in the case of CuCr_2Se_4 there is no intermediate approach between GGA and mBJ potential available, which would correctly describe the bands around Fermi level.

The dependence of the Nernst effect of CuCr_2S_4 , CuCr_2Se_4 , and CuCr_2Te_4 on the magnetic field is displayed for selected temperatures in the upper panels of Figs. 8, 9, and 10, respectively (see Figs. S2, S3, and S4 in Supplemental Material [32] for full hysteresis loops). The lower panels of Figs. 8 and 9 highlight the sign change of the ANE for CuCr_2S_4 and CuCr_2Se_4 , whereas the lower panel of Fig. 10 displays the vanishing of the ANE above $T_C \sim 325$ K for CuCr_2Te_4 . The total signal of the Nernst effect (S_{xyz}) is composed of the ordinary and anomalous contributions (S_{xyz}^O and S_{xyz}^A) according to the relation $S_{xyz} = S_{xyz}^O H + S_{xyz}^A (M)$. Whereas ordinary Nernst effect is linearly proportional to the applied magnetic field (H), the anomalous Nernst effect follows the field dependence of magnetization (M). The ordinary Nernst coefficient S_{xyz}^O was extracted as the slope of the linear extrapolation of the high field part of the hysteresis curves, and the constant part of the remaining curve was taken as the amplitude of ANE, see Fig. S5 in the Supplemental Material [32]. The extracted temperature dependence of the ANE are displayed in Fig. 11. The ANE is negative at room temperature for all phases, the highest absolute value $\sim 1.5 \mu\text{V/K}$ is ob-

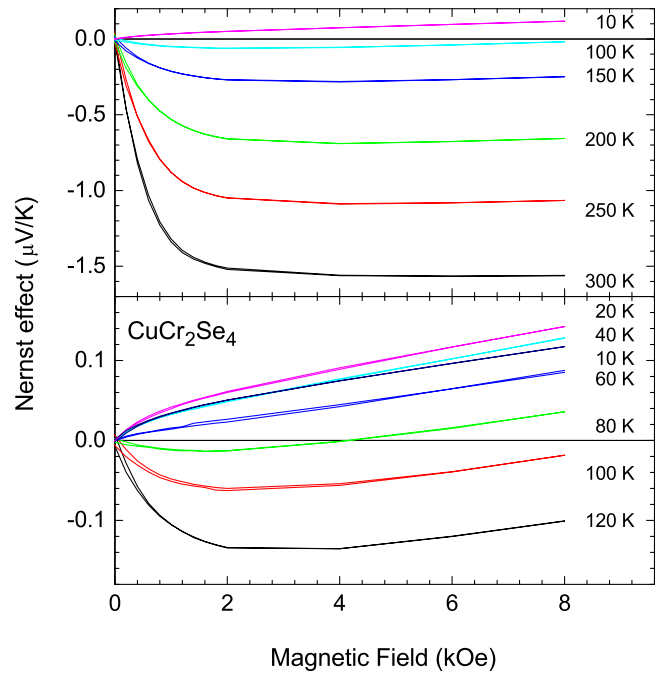


FIG. 9. Experimentally determined Nernst effect of CuCr_2Se_4 for selected temperature. The lower panel is focused on the sign change of ANE around 65 K.

served for $X = \text{Te}$ and Se around room temperature, whereas Nernst effect for $X = \text{S}$ is much smaller. A sign change of ANE to positive is observed at 285 K for $X = \text{S}$ and at 65 K for $X = \text{Se}$, see the inset of the Fig. 11 and lower panel of Fig. 8.

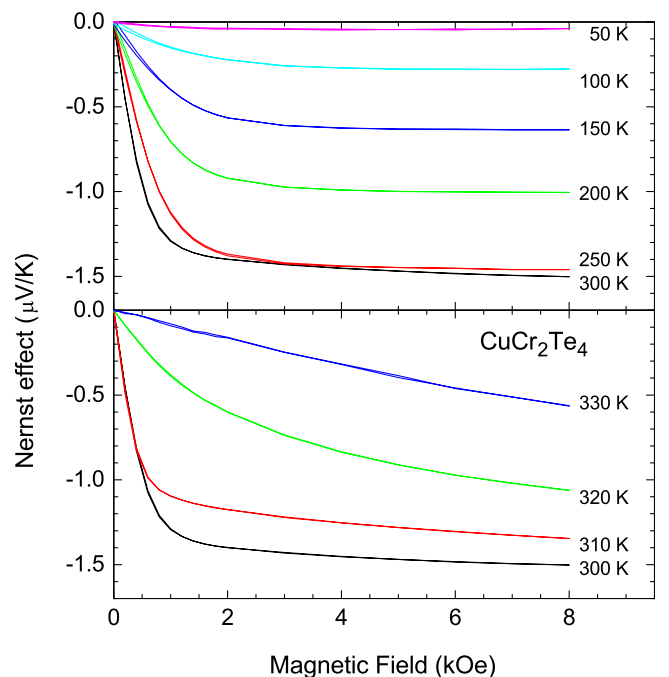


FIG. 10. Experimentally determined Nernst effect of CuCr_2Te_4 for selected temperature. The lower panel is focused on the vanishing of ANE above T_C .

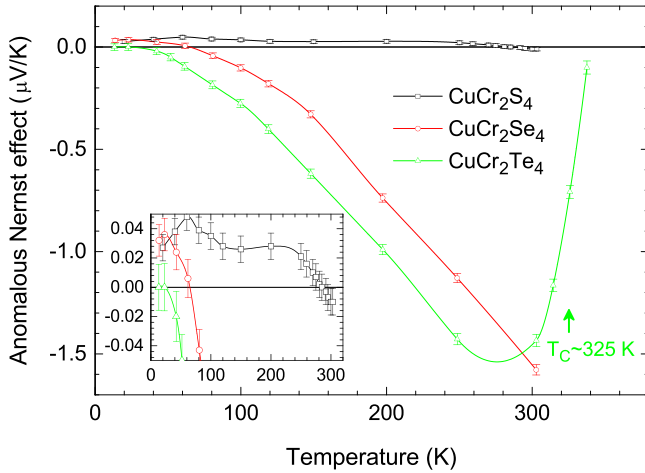


FIG. 11. Experimentally determined temperature dependence of anomalous Nernst effect for CuCr_2S_4 , CuCr_2Se_4 , and CuCr_2Te_4 . The inset highlights the sign changes of ANE.

It should be noted that the experiments were done in the adiabatic mode, i.e., with thermal current $Q_y = 0$.² This is different from the isothermal measurement with $\nabla_y T = 0$, for which the proper Nernst effect is measured. In adiabatic experiment a small thermal gradient $\nabla_y T$ arises necessarily in response to applied gradient $\nabla_x T$ due to the thermal Hall effect (or Righi-Leduc effect), see, e.g., [35–37]. Consequently, an additional contribution to the ANE signal that depends on Seebeck coefficient S_{xxz} and the ratio $\nabla_y T / \nabla_x T$ or the ratio of the transverse and longitudinal thermal conductivities ($\nabla_y T / \nabla_x T = \kappa_{xyz} / \kappa_{xxz}$) is given by the formula (see, e.g., Eq. (5.18) in Ref. [38])

$$S_{xyz}^A(\text{adiabatic}) = S_{xyz}^A(\text{isothermal}) - S_{yyz} \frac{\kappa_{xyz}}{\kappa_{xxz}}, \quad (4)$$

where we may put $S_{yyz} = S_{xxz}$ since our samples are isotropic (polycrystalline specimens without preferential orientation). In order to determine the correction of the ANE data, the value and sign of κ_{xyz} could be deduced from Hall conductivity data σ_{xyz} based on Wiedemann-Franz law $\kappa_{xyz} = L_o \sigma_{xyz} T$, where L_o is the Lorenz number $2.44 \times 10^{-8} \text{ W } \Omega \text{ K}^{-2}$, for experimental proof see [36]. The correction for anomalous thermal Hall effect (ATHE) can be neglected in most materials. Since the κ_{xyz} derived from the Wiedemann-Franz law is a response to the electronic part of thermal conductivity κ_{xxz} only, the ratio $\kappa_{xyz} / \kappa_{xxz}$ is negligible in insulators or semiconductors, where the phononic part of thermal conductivity is dominant over the electronic part. The electronic part of the thermal conductivity predominates in metals, but these in turn possess a small Seebeck coefficient. However, in the present case of CuCr_2Se_4 and CuCr_2Te_4 , these materials have high

²A small thermal current and consequently thermal gradient in y direction may be caused by a possible small misalignment of the heater relative to the center of the sample, but this thermal gradient will create a constant or symmetric signal in dependence on the magnetic field, which can be easily separated from the Nernst signal, see Fig. S5 for details.

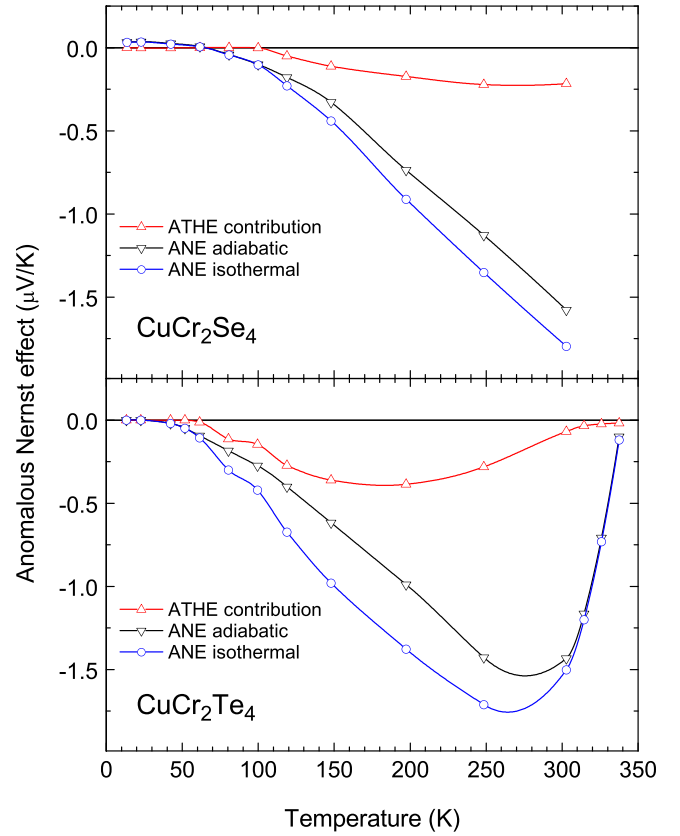


FIG. 12. The temperature dependence of experimentally determined adiabatic anomalous Nernst effect S_{xyz}^A (adiabatic), the contribution of the anomalous thermal Hall effect (ATHE), and the calculated S_{xyz}^A (isothermal), see Eq. (4), for CuCr_2Se_4 and CuCr_2Te_4 .

electric conductivity, and consequently the electronic part of thermal conductivity makes up to 50% of the total thermal conductivity (see Fig. S1 [32]), and at the same time they display high Seebeck coefficient due to the enhancement by the magnon drag. It appears that the contribution of ATHE is significant, namely up to $-0.2 \mu\text{V/K}$ for CuCr_2Se_4 and up to $-0.4 \mu\text{V/K}$ for CuCr_2Te_4 , see Fig. 12. Anomalous Hall resistivity ρ_{xyz}^A is positive for these materials, see Fig. S6 in the Supplemental Material [32], so anomalous Hall conductivity calculated using the formula $\sigma_{xyz} = -\rho_{xyz} / (\rho_{xxz}^2 + \rho_{xyz}^2)$ is negative, thus κ_{xyz} is also negative, and in total the correction term $-S_{xxz} \kappa_{xyz} / \kappa_{xxz}$ is positive. Therefore, the corrected S_{xyz}^A (isothermal) is in absolute values enhanced compared to the experimental ANE S_{xyz}^A (adiabatic), in particular within the temperature range $\approx 100\text{--}300 \text{ K}$. But the contribution of ATHE does not alter the general shape of the temperature dependence of ANE as well as has no influence on the sign change of ANE around 65 K for CuCr_2Se_4 , as at this temperature the ATHE contribution to ANE is negligible. In the case of CuCr_2S_4 , the calculated contribution of ATHE is less than $10^{-3} \mu\text{V/K}$ over the whole experimental temperature range.

For the sake of comparison of the experimental and calculated transverse thermal properties, in the first step we have calculated anomalous Hall conductivity (AHC) using Eq. (1). Figure 13 shows the calculated AHC of CuCr_2X_4 at zero temperature in dependence on the chemical potential

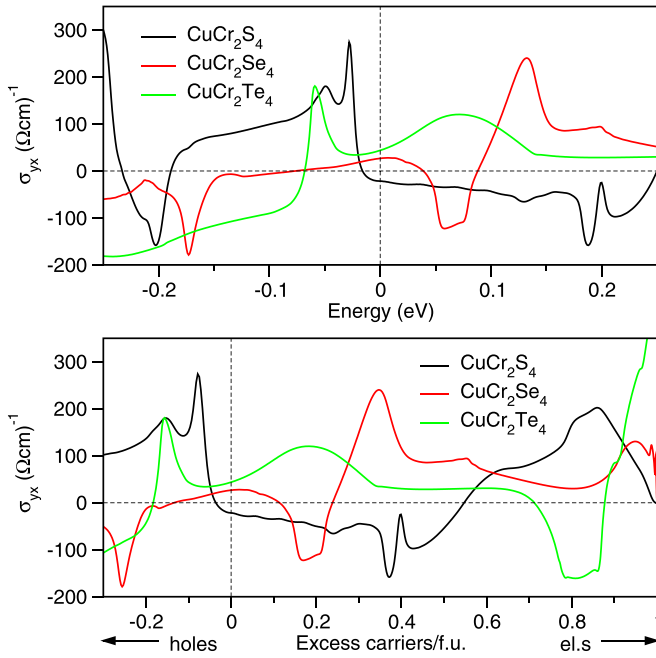


FIG. 13. Calculated anomalous Hall conductivity of CuCr_2X_4 in dependence on the chemical potential and doping.

and hole/electron doping. Our calculations are in agreement with the theoretical analysis performed for $\text{CuCr}_2\text{Se}_{4-x}\text{Br}_x$ system in Ref. [8], namely it reproduces the sign changes with electron doping. In the next step the temperature dependence of the anomalous Nernst conductivity (ANC) was calculated from AHC using Eq. (2). The experimental ANC α_{xyz}^A was derived from longitudinal electrical conductivity σ_{xxz} , anomalous Nernst effect S_{xyz}^A , Seebeck coefficient S_{xxz} , and anomalous Hall conductivity σ_{xyz}^A using the formula $\alpha_{xyz}^A = \sigma_{xxz}S_{xyz}^A + \sigma_{xyz}^AS_{xxz}$, applicable for our isotropic system. The temperature dependence of the experimental and calculated ANC is displayed in Fig. 14.

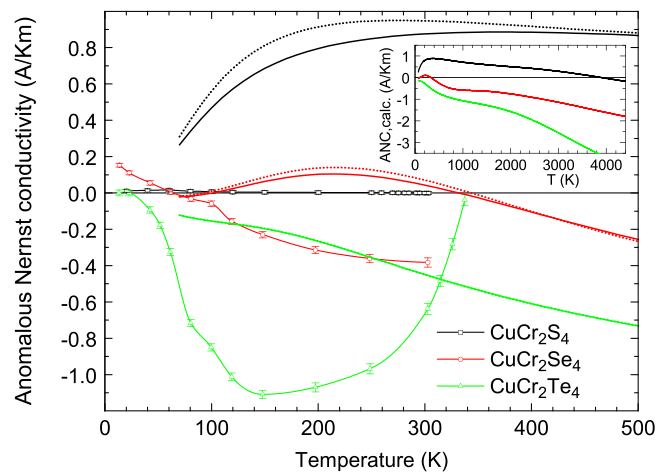


FIG. 14. Comparison of experimental and calculated anomalous Nernst conductivity $\alpha_{xyz}^A = \sigma_{xxz}S_{xyz}^A + \sigma_{xyz}^AS_{xxz}$ of CuCr_2S_4 , CuCr_2Se_4 , and CuCr_2Te_4 . Full line for calculated ANC with variable chemical potential, dotted line for fixed chemical potential.

Let us note that ANC obtained using Eq. (2) is actually calculated with chemical potential μ fixed at the position for $T = 0$ K (dotted lines in Fig. 14). However, chemical potential is usually not constant with increasing temperature unless it is exactly in the middle of the symmetric band. Therefore we have also calculated ANC using the evolution of μ with temperatures adopted from the BOLTZTRAP output, see the solid lines in Fig. 14. Nevertheless, it can be seen that the difference between ANC calculated with fixed and variable μ can be considered as negligible.

The calculated ANC follows a similar trend as the experimental ANC in the sense that it reproduces correctly the change from positive values for $X = \text{S}$ and Se to negative for $X = \text{Te}$ at low temperature and sign change to negative for $X = \text{S}$ and Se at higher temperature. However, the calculated sign changes occurs at much higher temperatures than observed, see the inset of Fig. 14. We propose the following arguments for the explanation of the difference in the temperature scales of the experimental and calculated ANC. The comparison of calculated and experimental results of Seebeck coefficients shown above indicate that our band structure has a correct dispersion around the Fermi energy. On the other hand, the Berry curvature is calculated using the whole range of the occupied bands, from the bottom of the spin-polarized bands (-7 eV) to the Fermi energy. It means that, in distinction to Seebeck coefficient, calculated AHC (and subsequently ANC) is affected by band structure dispersion not only near E_F , but also by the lower occupied bands. In principle, the strong correlation effects of d electrons yield bandwidth renormalization, namely narrowing of the bands, which cannot be evaluated by the DFT approach. To include such many-body physics (changes of the effective mass of quasiparticles), methods like, e.g., dynamical mean-field theory calculations has to be used. Since there is a strong hybridization between metal d orbitals and ligand p orbitals, the bands around E_F are less affected by renormalization effects. However, the bands display a dominant d character within the range from -4 to -1 eV below E_F , where a bigger correction by the strong correlation effects is anticipated, see the projected DOS in Fig. S7 in the Supplemental Material [32]. The renormalization might be different for each phase depending on the degree of correlation effect, presumably increasing from $X = \text{Te}$ to S . The renormalization of the band structure within this energy range would result in contraction of the temperature scale of calculated ANC, and would give better agreement of the calculated and experimental ANC, but will not affect the calculation of the Seebeck coefficient.

The vanishing of ANC toward zero above T_C for $X = \text{Te}$ is not reproduced by Berry phase calculation, since it uses the band structure corresponding to the perfect magnetic ordering at 0 K, so it does not take into account lowering magnetization with increasing temperature and finally vanishing magnetization and ANC above T_C . The critical temperature for $X = \text{S}$ and Se is above the temperature range for Nernst effect measurement, so it is not reflected in the data.

For the possible thermoelectric applications it is interesting that the magnitude of the Nernst effect increases from $X = \text{S}$ to Te (opposite to trend in Seebeck coefficient), i.e., it displays the same trend as the electrical conductivity. Thus in the case of the “longitudinal” thermoelectric power factor

$P_{xxz} = S_{xxz}^2 \sigma_{xxz}$ the increase of conductivity is compensated by the decrease of Seebeck from $X = \text{S}$ to Te , whereas for the “transverse” power factor, which could be defined as $P_{xyz} = S_{xyz}^2 \sigma_{xyz}$ (assuming $\sigma_{xxz} = \sigma_{yyz}$), both electrical conductivity and Nernst effect exhibit the same trend of increasing from $X = \text{S}$ to Te . However, the possible application of the Nernst effect of CuCr_2Te_4 is limited by the rather low critical temperature of the long range magnetic ordering.

V. CONCLUSIONS

The transport properties of ferrimagnetic spinels CuCr_2X_4 ($X = \text{S, Se, Te}$) were investigated both experimentally and theoretically by the DFT methods. The thermoelectric power of all studied phases is positive and consists of two contributions; an almost linear diffusive thermopower observed at high temperature, and a strong enhancement by magnon drag below T_C . The diffusive part of the thermoelectric power was calculated using WIEN2K package and BOLTZTRAP program. The agreement with experiment was tested for several selected potentials, namely GGA, GGA + U , GGA+oeeHyb, and mBJ. The best agreement with the experimental thermoelectric power was achieved using GGA potential for $X = \text{S}$ and with mBJ potential for $X = \text{Te}$. We explained these results by a stronger sp -orbitals character of the valence bands of CuCr_2Te_4 compared to sulfide and selenide, in coherency with the designation of the mBJ potential for improving the description of band structure and band gaps of sp -type semiconductors.

The transverse thermoelectric properties represented by the Nernst effect were measured for CuCr_2S_4 and CuCr_2Te_4 and compared with the measurement for well known CuCr_2Se_4 . The anomalous Nernst effect is negative at room temperature for all phases. The highest absolute value up to $\sim 1.5 \mu\text{V}/\text{K}$ is observed for $X = \text{Te}$, but it is exceeded by ANE of $X = \text{Se}$ at room temperature due to lower T_C of CuCr_2Te_4 . The Nernst effect for $X = \text{S}$ is much smaller. A sign change of ANE to positive is observed at 285 K for $X = \text{S}$ and at 65 K for $X = \text{Se}$. The trend of anomalous Nernst conductivity is reproduced by Berry phase calculations if the renormalization of the bands due to the strong correlation effects is taken into account.

For the possible thermoelectric applications it is important that the magnitude of the Nernst effect displays the same trend as the electrical conductivity, i.e., increases from $X = \text{S}$ to Te (opposite to trend in Seebeck coefficient). However, the possible application of the Nernst effect of CuCr_2Te_4 is limited by the rather low ferrimagnetic T_C .

ACKNOWLEDGMENTS

The financial support from the Czech Science Foundation Projects No. 19-06433S and No. 18-12761S is acknowledged.

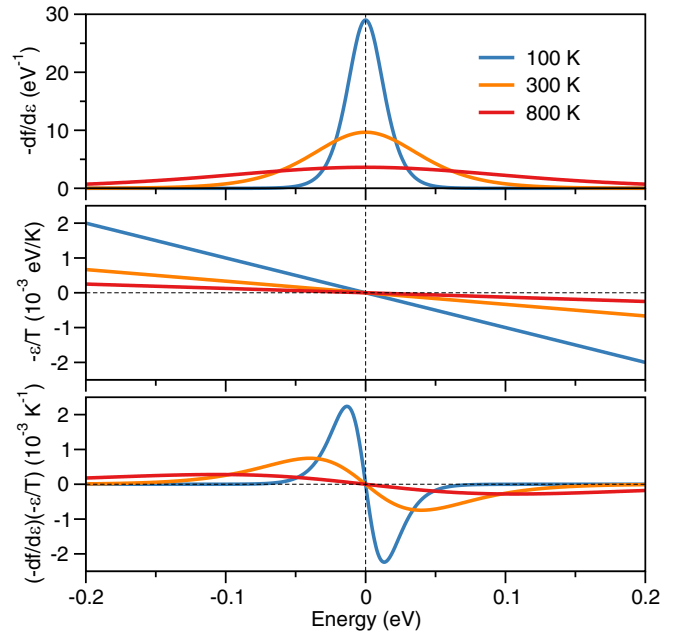


FIG. 15. Plots of $-\partial f/\partial \varepsilon$, $-\varepsilon/T$, and $(-\partial f/\partial \varepsilon)(-\varepsilon/T)$ for the three selected temperatures of 100, 300, and 500 K.

Computational resources were supplied by the project e-Infrastruktura CZ (e-INFRA LM2018140) provided within the program Projects of Large Research, Development and Innovations Infrastructures. The experiments were performed at Materials Growth & Measurement Laboratory (MGML) [39], which is supported within the program of Czech Research Infrastructures (Project No. LM2018096). Valuable discussions with Z. Jiráček are gratefully acknowledged.

APPENDIX: ANALYTIC UNDERSTANDING OF ANC

In this Appendix we explain how the T -dependent α_{xyz} is calculated from the σ_{xyz} at zero temperature. Assuming $\mu = 0$, for simplicity, the equation of α_{xyz} can be rewritten as

$$\alpha_{xyz}(T) = \frac{1}{e} \int_{-\infty}^{\infty} d\varepsilon \left(-\frac{\partial f}{\partial \varepsilon} \right) \left(-\frac{\varepsilon}{T} \right) \sigma_{xyz}(0, \varepsilon). \quad (\text{A1})$$

There are three parts in the integral: $-\partial f/\partial \varepsilon$ for the Gaussian function, $-\varepsilon/T$ for the linear contribution of ε , and σ_{xyz} at zero temperature. In this formalism, only the part $(-\partial f/\partial \varepsilon)(-\varepsilon/T)$ has the complete information of T -dependent dynamics. The factor behaves as the weight function for $\sigma_{xyz}(0, \varepsilon)$, which decides the contributions to α_{xyz} in the integral, i.e., the positive (negative) part of the scale factor is multiplied to σ_{xyz} at $\varepsilon < 0$ ($\varepsilon > 0$), see the curves calculated for selected temperatures in Fig. 15. Also the structure of σ_{xyz} near $\varepsilon \sim 0$ plays a more important role than the value at $\varepsilon = 0$ itself.

[1] V. V. Tsurkan and S. I. Radutsan, Peculiarities of galvanomagnetic effects in ternary magnetic CuCr_2X_4 single-crystals

near magnetic phase-transition, *Jpn. J. Appl. Phys.* **32**, 313 (1993).

- [2] W. L. Lee, S. Watauchi, V. L. Miller, R. J. Cava, and N. P. Ong, Anomalous Hall Heat Current and Nernst Effect in the $\text{CuCr}_2\text{Se}_{4-x}\text{Br}_x$ Ferromagnet, *Phys. Rev. Lett.* **93**, 226601 (2004).
- [3] W. L. Lee, S. Watauchi, V. L. Miller, R. J. Cava, and N. P. Ong, Dissipationless anomalous Hall current in the ferromagnetic spinel $\text{CuCr}_2\text{Se}_{4-x}\text{Br}_x$, *Science* **303**, 1647 (2004).
- [4] D. Xiao, Y. G. Yao, Z. Fang, and Q. Niu, Berry-Phase Effect in Anomalous Thermoelectric Transport, *Phys. Rev. Lett.* **97**, 026603 (2006).
- [5] J. S. Bettinger, R. V. Chopdekar, M. Liberati, J. R. Neulinger, M. Chshiev, Y. Takamura, L. M. B. Alldredge, E. Arenholz, Y. U. Idzerda, A. M. Stacy, W. H. Butler, and Y. Suzuki, Magnetism and transport of CuCr_2Se_4 thin films, *J. Magn. Magn. Mater.* **318**, 65 (2007).
- [6] W. X. Feng, C. C. Liu, G. B. Liu, J. J. Zhou, and Y. G. Yao, First-principles investigations on the Berry phase effect in spin-orbit coupling materials, *Comput. Mater. Sci.* **112**, 428 (2016).
- [7] K. Oda, S. Yoshii, Y. Yasui, M. Ito, T. Ido, Y. Ohno, Y. Kobayashi, and M. Sato, Unusual anomalous Hall resistivities of CuCr_2S_4 , $\text{Cu}_{0.5}\text{Zn}_{0.5}\text{Cr}_2\text{Se}_4$ and Cr_3Te_4 , *J. Phys. Soc. Jpn.* **70**, 2999 (2001).
- [8] Y. G. Yao, Y. C. Liang, D. Xiao, Q. Niu, S. Q. Shen, X. Dai, and Z. Fang, Theoretical evidence of the Berry-phase mechanism in anomalous Hall transport: First-principles studies of $\text{CuCr}_2\text{Se}_{4-x}\text{Br}_x$, *Phys. Rev. B* **75**, 020401(R) (2007).
- [9] L. Onsager, Reciprocal relations in irreversible processes I, *Phys. Rev.* **37**, 405 (1931).
- [10] L. Onsager, Reciprocal relations in irreversible processes II, *Phys. Rev.* **38**, 2265 (1931).
- [11] H. B. Callen, The application of Onsager's reciprocal relations to thermoelectric, thermomagnetic, and galvanomagnetic effects, *Phys. Rev.* **73**, 1349 (1948).
- [12] N. F. Mott and H. Jones, *The Theory of the Properties of Metals and Alloys* (Dover, New York, 1958).
- [13] T. S. Tripathi, G. C. Tewari, and A. K. Rastogi, The study of magnon-drag effects in the thermopower of CuCr_2X_4 ($X = \text{S}, \text{Se}$ and Te), *J. Phys.-Conf. Ser.* **200**, 032060 (2010).
- [14] T. S. Tripathi and M. Karppinen, Experimental setup for anisotropic thermoelectric transport measurements using MPMS, *Meas. Sci. Technol.* **30**, 025602 (2019).
- [15] M. Robbins, H. W. Lehmann, and J. G. White, Neutron diffraction and electrical transport properties of CuCr_2Se_4 , *J. Phys. Chem. Solids* **28**, 897 (1967).
- [16] C. Colominas, Neutron-diffraction investigation of CuCr_2Se_4 and CuCr_2Te_4 , *Phys. Rev.* **153**, 558 (1967).
- [17] D. Rodic, B. Antic, R. Tellgren, H. Rundlof, and J. Blanus, A change of magnetic moment of Cr ion with the magnetic phase transition in CuCr_2Se_4 , *J. Magn. Magn. Mater.* **187**, 88 (1998).
- [18] O. Yamashita, Y. Yamaguchi, I. Nakatani, H. Watanabe, and K. Masumoto, Polarized neutron-diffraction study of a CuCr_2Se_4 single-crystal, *J. Phys. Soc. Jpn.* **46**, 1145 (1979).
- [19] G. K. Madsen, J. Carrete, and M. J. Verstraete, BoltzTraP: A code for calculating band-structure dependent quantities, *Comp. Phys. Commun.* **231**, 140 (2018).
- [20] R. F. W. Bader, *Atoms in Molecules: A Quantum Theory* (Oxford University Press, Oxford, 1994).
- [21] P. Blaha, K. Schwarz, F. Tran, R. Laskowski, G. K. H. Madsen, and L. D. Marks, WIEN2k: An APW+lo program for calculating the properties of solids, *J. Chem. Phys.* **152**, 074101 (2020).
- [22] J. P. Perdew, K. Burke, and M. Ernzerhof, Generalized Gradient Approximation Made Simple, *Phys. Rev. Lett.* **77**, 3865 (1996).
- [23] F. Tran and P. Blaha, Accurate Band Gaps of Semiconductors and Insulators with a Semilocal Exchange-Correlation Potential, *Phys. Rev. Lett.* **102**, 226401 (2009).
- [24] F. Tran, P. Blaha, K. Schwarz, and P. Novák, Hybrid exchange-correlation energy functionals for strongly correlated electrons: Applications to transition-metal monoxides, *Phys. Rev. B* **74**, 155108 (2006).
- [25] A. D. Becke and E. R. Johnson, A simple effective potential for exchange, *J. Chem. Phys.* **124**, 221101 (2006).
- [26] M. T. Czyżyk and G. A. Sawatzky, Local-density functional and on-site correlations: The electronic structure of La_2CuO_4 and LaCuO_3 , *Phys. Rev. B* **49**, 14211 (1994).
- [27] J. Kuneš, R. Arita, P. Wissgott, A. Toschi, H. Ikeda, and K. Held, Wien2wannier: From linearized augmented plane waves to maximally localized Wannier functions, *Comp. Phys. Commun.* **181**, 1888 (2010).
- [28] A. A. Mostofi, J. R. Yates, G. Pizzi, Y.-S. Lee, I. Souza, D. Vanderbilt, and N. Marzari, An updated version of Wannier90: A tool for obtaining maximally-localised Wannier functions, *Comp. Phys. Commun.* **185**, 2309 (2014).
- [29] X. Wang, J. R. Yates, I. Souza, and D. Vanderbilt, *Ab initio* calculation of the anomalous Hall conductivity by Wannier interpolation, *Phys. Rev. B* **74**, 195118 (2006).
- [30] I. Nakatani, H. Nosé, and K. Masumoto, Magnetic properties of CuCr_2Se_4 single crystals, *J. Phys. Chem. Solids* **39**, 743 (1978).
- [31] N. Nagaosa, J. Sinova, S. Onoda, A. H. MacDonald, and N. P. Ong, Anomalous Hall effect, *Rev. Mod. Phys.* **82**, 1539 (2010).
- [32] See Supplemental Material at <http://link.aps.org/supplemental/10.1103/PhysRevB.104.085146> for figures with (a) total and electronic part of thermal conductivity, (b) full hysteresis loops of the Nernst effect, (c) analysis of the Nernst effect raw hysteresis loops, (d) anomalous Hall resistivity, and (e) projected DOS.
- [33] I. Pallecchi, F. Caglieris, and M. Putti, Thermoelectric properties of iron-based superconductors and parent compounds, *Superconduct. Sci. Technol.* **29**, 073002 (2016).
- [34] B. Flebus, R. A. Duine, and Y. Tserkovnyak, Landau-Lifshitz theory of the magnon-drag thermopower, *Europhys. Lett.* **115**, 57004 (2016).
- [35] Y. Shiomi, Y. Onose, and Y. Tokura, Extrinsic anomalous hall effect in charge and heat transport in pure iron, $\text{Fe}_{0.997}\text{Si}_{0.003}$, and $\text{Fe}_{0.97}\text{Co}_{0.03}$, *Phys. Rev. B* **79**, 100404(R) (2009).
- [36] Y. Shiomi, Y. Onose, and Y. Tokura, Effect of scattering on intrinsic anomalous Hall effect investigated by Lorenz ratio, *Phys. Rev. B* **81**, 054414 (2010).
- [37] X. Li, L. Xu, L. Ding, J. Wang, M. Shen, X. Lu, Z. Zhu, and K. Behnia, Anomalous Nernst and Righi-Leduc Effects in Mn_3Sn : Berry Curvature and Entropy Flow, *Phys. Rev. Lett.* **119**, 056601 (2017).
- [38] H. B. Callen, A note on the adiabatic thermomagnetic effects, *Phys. Rev.* **85**, 16 (1952).
- [39] <http://mgml.eu>.